Group 4 Final Project

Jacob Johnston (*jmj3957*)
Trevor Lease (*tal2434*)
Braden Pecora (*bsp825*)

University of Texas at Austin
COE 347

May 15, 2022

1 Objective

The objective of this paper is to compare the analytical and computational solutions for an inviscid supersonic flow around a diamond airfoil for various angles of attack and Mach numbers. Some key parameters of flow we will compare are the lift and drag coefficients, as well as the shock angle. Additionally, we will use meshes of varying resolution to ensure the convergence of the numerical solution to the analytical solution.

2 Introduction

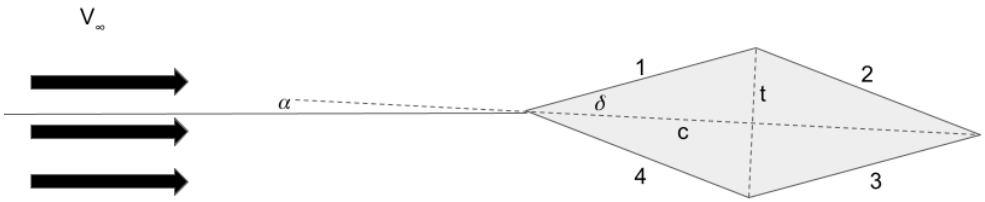

Figure 1: Schematic of the Diamond airfoil in general form.

For this project, inviscid supersonic flow was simulated around a diamond airfoil. The general diamond airfoil geometry is determined by a half vertex angle δ, an angle of attack α, and a half-chord length c (Figure 1).

Mach number is defined as the ratio between the local velocity, V, and the speed of sound, a. The local mach number at a point is

$$M = \frac{V}{a}, \tag{1}$$

where the speed of sound, a, is defined as

$$a = \sqrt{\gamma RT}. \tag{2}$$

For our analysis, the simulated fluid was normalized, meaning that the temperature and pressure at the inlet (and throughout the fluid at $t = 0$) were 1 K and 1 Pa respectively. Additionally, the ratio of specific heats, γ, was set to be 1.4 and universal gas constant, R, was 8314 J/kmol-K. Therefore, we prescribed a molecular weight 11640 g/mol to the fluid such that Equation 2 was equal to 1 at the inlet where $T = 1$ K. Thus, a velocity of 3m/s at the inlet would correspond to Mach 3 flow. Finally, the values for γ, R, and the molecular weight determined the specific heat at constant pressure, c_p, to be 2.5 J/kg-K.

Angle of attack, α, is the angle between the incoming flow and the chord of the diamond airfoil. Positive values of α are in the upwards direction, and negative values correspond to the the downwards direction.

Figure 1 illustrates the relationship between the geometry of the diamond airfoil and how each variable was defined. The thickness, t, is the dimension of the half-height of the diamond airfoil and the chord length, c, is the half-length of the diamond airfoil. Both of these variables are in relation to the vertex points.

The half-vertex angle, δ, can be defined in terms of t and c:

$$\delta = \arctan\left(\frac{t}{c}\right). \tag{3}$$

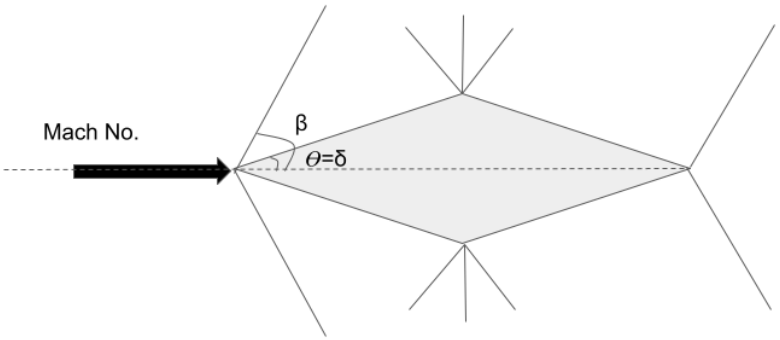

Figure 2: Relationship of Turn angle and shock angle

The deflection angle, θ, is the angle at which the incoming flow turns. For our simulations, the incoming flow from the inlet must turn in order to satisfy the boundary conditions imposed at the location of the airfoil, which is that the flow must be parallel to the foil at the boundary between the foil and the fluid. For simplicity, let us consider $\alpha = 0$, as shown in Figure 2. In this case, the deflection angle is equal to the half vertex angle. In other words, the incoming flow only has to turn at an angle equivalent to half of the vertex angle. If we increase the angle of attack, then the turn angle would be

$$\theta = \delta \pm \alpha \tag{4}$$

The plus/minus sign indicates that the turn angle will be different on the top and bottom surfaces. The plus sign indicates the turn angle of the bottom surface, while the minus sign indicates the turn angle on the top surface. This will be the main case considered going forward in this report.

(a) Into (b) Away

Figure 3: Flow turning into and away from itself

To predict if an oblique shock or expansion fan will form on the diamond airfoil, one must consider which direction the flow is turning. If the flow has a turn angle in which it is turning "into" itself, as shown in Figure 9a, an oblique shock will form at the turn. If the flow has a turn angle in which it is turning "away" from itself, as shown in Figure 9b, an expansion fan will form at the turn. This will help predict what the CFD model should be producing for various angle of attacks and can help ensure that the mesh and simulations are in accordance with analytical solutions.

The first two key paramters that we will calculate from the flow are the lift and drag coefficients. Assuming an inviscid flow, it can be shown that the coefficients of lift and drag per unit span are a function of the freestream Mach number, the wedge half angle, and the angle of attack, and can be computed by the following expression. In this paper, we will express the coefficients of lift and drag together as a complex number, with the real part equal to the lift coefficient and the imaginary part equal to the drag coefficient.

$$C_f = C_l + iC_d = \frac{(P_4 - P_2)e^{i(\delta+\alpha)} + (P_3 - P_1)e^{-i(\delta-\alpha)}}{P_\infty M^2 \gamma} \sec\delta \tag{5}$$

While we expressed the complex force coefficient in terms of the four surface pressures, these are functions of M, θ, and α as well and can be determined using shock-expansion theory.

Additionally, we will investigate the shock angle for various flow parameters. Theta-Beta-M curves are a graphical form of the relationship between the turn angle θ, the Mach number, M, and the angle of the oblique shock β.

Mathematically, the relationship between θ, β, and M is as follows:

$$\tan(\theta) = 2\cot\beta\left(\frac{M^2\sin^2(\beta) - 1}{M^2(\gamma + \cos(2\beta)) + 2}\right). \tag{6}$$

Examples of $\theta\beta M$ curves are shown for various Mach numbers in Figure 4. It is important to note that for each combination of θ and M, there are two values for β. This is because Equation 6 actually yields two solutions for β for each (θ,M) pair. The higher value of β is known as the strong shock solution, which occurs when the oblique shock causes velocity to transition from supersonic to subsonic. The lower β value is known as the weak shock solution. The weak shock solution occurs when the flow remains supersonic before and after the shock. The strong shock solutions are extremely rare in

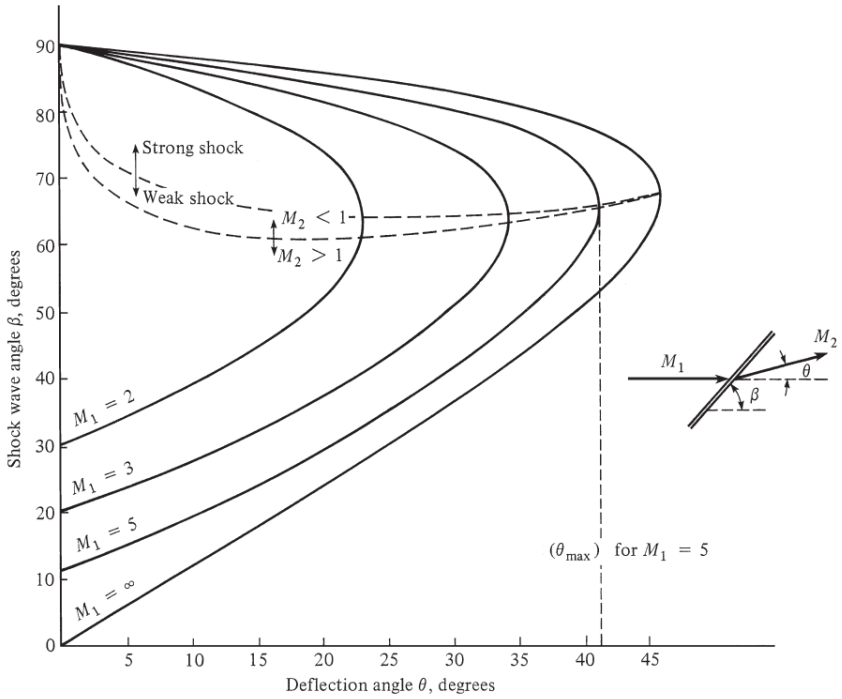

Figure 4: θ-β-M curve (Anderson 137)

practical settings and outside of the scope of the diamond-airfoil case. For this paper, only the weak shock solutions will be considered.

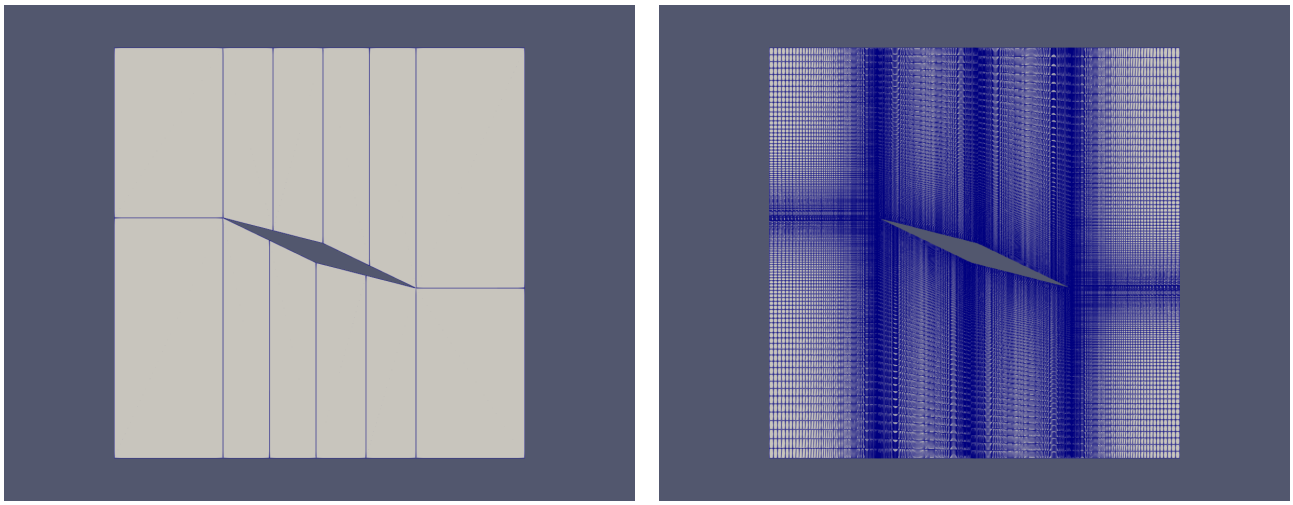

(a) Blocks (b) Cells

Figure 5: An example of the mesh used. Block vertices are relative to airfoil vertices/midpoints between vertices, which allows for consistency across a variety of angle of attacks and diamond foil geometries.

3 Mesh Design

Designing a mesh for a diamond airfoil at variable angles of attack was more difficult than anticipated. High resolutions in regions of interest (around edge of the airfoil, particularly near the corners) was needed, and we had to keep each cell relatively orthogonal for all angles of attack. Hexahedrons were the only cell shape considered, which made the design process even more challenging.

For this project, several mesh designs were considered and used in simulations. We first considered a mesh that had diamond-shaped region of high resolution around the airfoil. We quickly found out that this mesh design resulted in highly-skewed cells, which decreased the accuracy of the simulation and increased the runtime.

A simpler mesh was also considered. This mesh had lines extending from each corner of the foil, which divided the domain into eight blocks. However, this mesh did not allow us to increase the resolution in the regions of interest without also increasing the resolution throughout most of the domain. This resulted in increased run times and large files sizes.

The mesh that we chose to use in our analysis is shown in Figure 5. This mesh is a variant of the simple mesh described in the previous paragraph, but the inner blocks were divided even further to allow for more control of grid refinement. With this mesh, the resolution around the corners of the foil could be increased without unnecessarily increasing the resolution between the corners.

At large angles of attack, the cells in this mesh can still become highly skewed. However, these large angles of attack were not considered for our analysis. The resulting flow of high-speed large-angle scenarios causes phenomena outside the scope of this project. We did attempt to simulate these flows with the `rhoCentralFoam` solver by using fine meshes and small timesteps, but it seems the solver is not equipped well for these scenarios (the fluid experiences large decreases in temperature and pressure, bow shocks form).

4 Lift and Drag

While the lift and drag for an arbitrary diamond airfoil can be computed from Equation 5, this equation assumes a constant pressure along a surface. However, since the numerical solution does not match the analytical solution exactly, we should not make this assumption. However, we can easily adapt Equation 5 for a non constant pressure distribution along the faces of the airfoil. The total force per unit span can be written as follows.

$$\vec{f} = -\oint P \cdot \vec{n} dl \tag{7}$$

If we interpret the surface normal vector as a complex number, with the real portion equalling the x-component of the vector and the imaginary portion equalling the y-component of the vector, we can approximate the complex force as:

$$f = \{\sum_{4}(P_{i,4}\delta x) - \sum_{2}(P_{i,2}\delta x)\}e^{i(\delta+\alpha)} + \{\sum_{3}(P_{i,3}\delta x) - \sum_{1}(P_{i,1}\delta x)\}e^{-i(\delta-\alpha)} \tag{8}$$

The complex force coefficient can then be computed using the following equation.

$$C_f = \frac{f}{P_\infty M^2 \gamma c} \tag{9}$$

In the case of a constant pressure along the surface, the above equation simplifies to Equation 5.

Three Mach numbers ($M = 3, 4, 5$) were tested for six negative angles of attack each. Since the angle of attack was negative, the lift coefficient was also negative. However, since the flow is symmetrical about the diamond airfoil:

$$C_l(\alpha) = -C_l(-\alpha) \tag{10}$$

$$C_d(\alpha) = C_d(-\alpha) \tag{11}$$

Therefore, all angles and lift coefficients were plotted as positive numbers. Figure 6 below shows the lift and drag coefficients as a function of the angle of attack for the three Mach numbers.

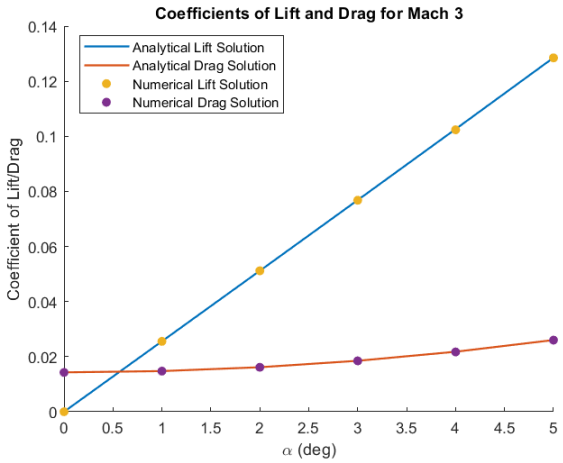

(a) $M = 3$

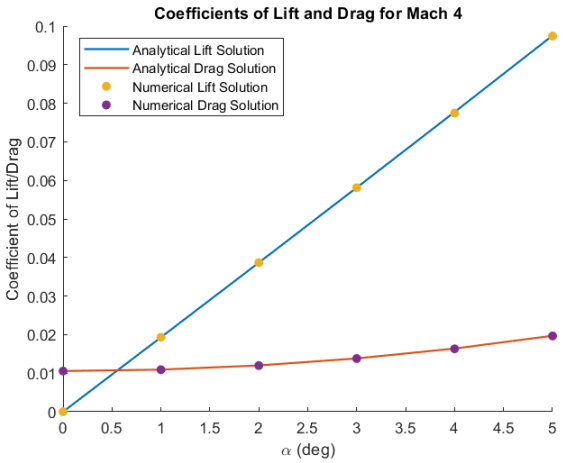

(b) $M = 4$

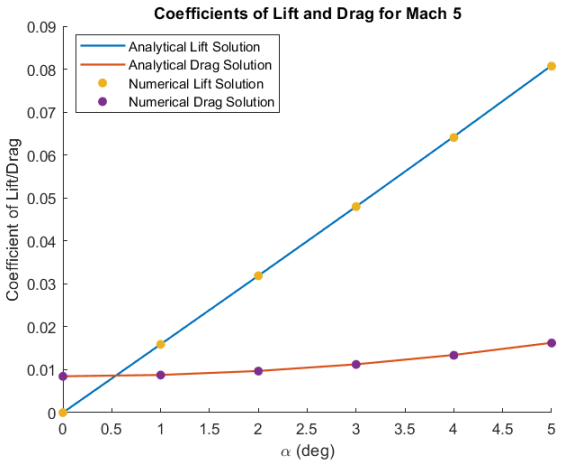

(c) $M = 5$

Figure 6: Lift and Drag Coefficients

The lift and drag coefficients are seen to match the analytical solution almost exactly for all Mach numbers and angles of attack.

For our convergence study, the Mach number will be held constant at $M = 3$ and $\alpha = 0$, and the number of cells in each direction were scaled by the same factor in each direction. Additionally, the timestep of the solver was adjusted to keep the Courant number constant as well. The drag coefficient was used as an error metric, with the error between the numerical solution and the analytical solution being defined as seen below, where C_d is the coefficient of drag of the analytical solution and C_d, n is the coefficient of drag of the numerical solution:

$$\epsilon = \frac{|C_d - C_{d,n}|}{C_d} \tag{12}$$

The error of the solution with respect to the number of cells can be seen below in Figure 7.

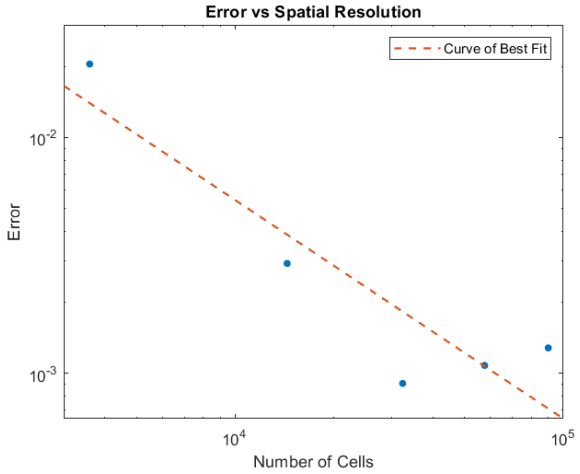

Figure 7: Error of the Solution with Respect to Number of Cells

It can be seen that the error of the solution generally decreases with higher resolution meshes. For the largest two simulations, however, the error actually increases slightly. This is mostly likely due to numerical errors associated with small cells sizes. We can also see convergence of the solution when comparing the pressure distributions along the top two surfaces to the analytical solution, as seen below in Figure 8.

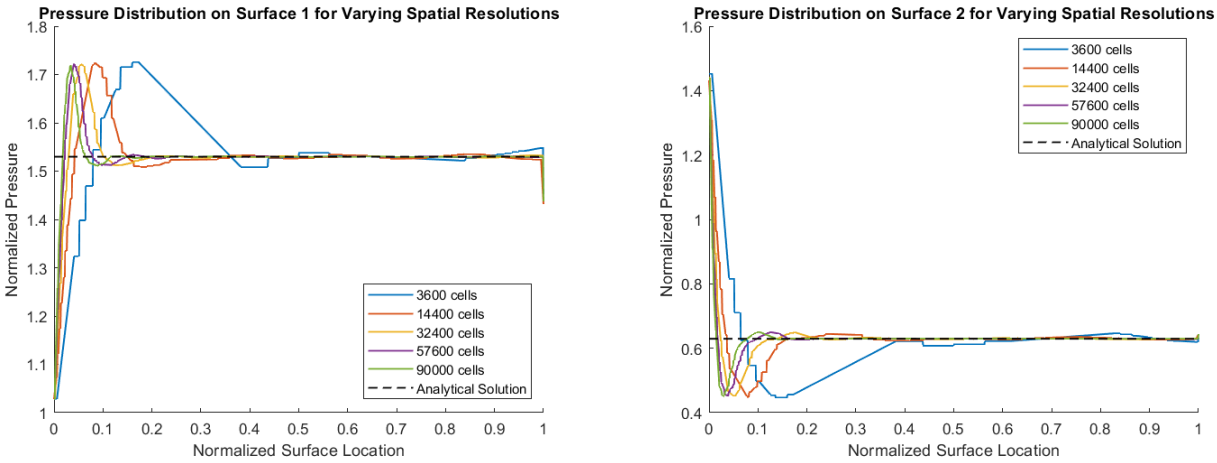

(a) Pressure Distribution on Surface 1

(b) Pressure Distribution on Surface 2

Figure 8: Surface Pressure Convergence

None of the pressure distributions match the analytical solution exactly, but the quality of the numerical solution increases with higher mesh resolutions. While shock-expansion theory predicts that the surface pressures will be constant across any given surface, the solution scheme that `rhoCentralFoam` adopts makes this impossible. Essentially, the solver "smears" abrupt changes in flow quantities over several cells, which is why an overshoot of the numerical pressure compared to analytical solution is seen for simulations. This region of overshoot, however, decreases with increasing number of cells, indicating that the width of the shock and expansion regions decrease with increasing spatial resolution.

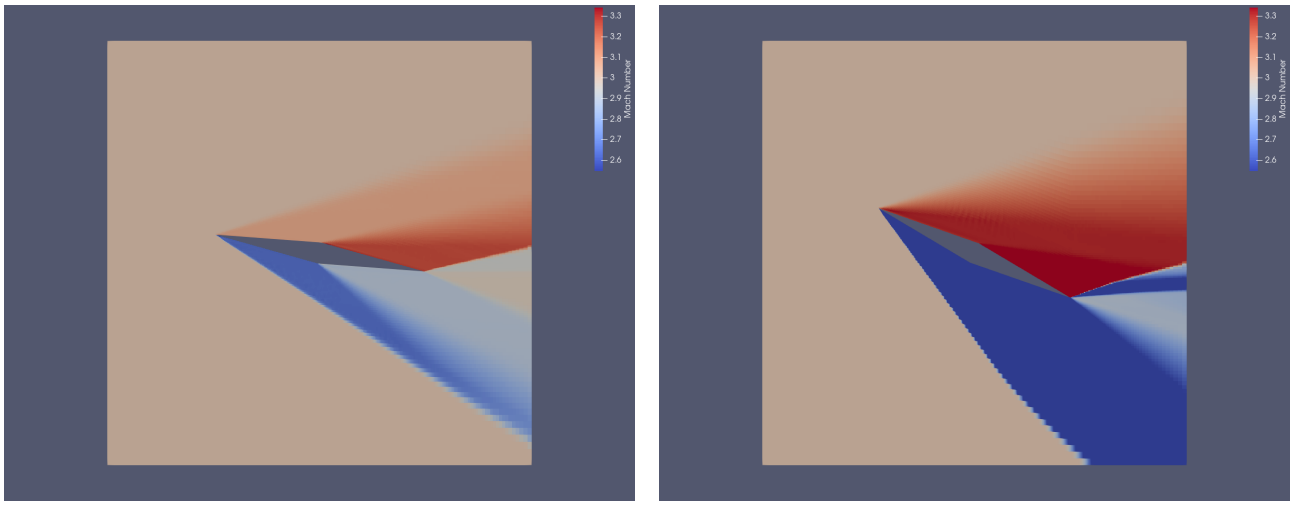

(a) Angle of Attack = 10°

(b) Angle of Attack = 25°

Figure 9: Example solutions (at Mach 3 inlet flow) with various angles of attack showcasing various shock wave angles.

5 Calculating Beta

From 9, it can be seen that shocks and expansion regions form where expected according to shock-expansion theory. To verify that `rhoCentralFoam` produces shocks at accurate β angles for various (θ, M) pairs (in agreement with Equation 6), several simulations were run with different combinations of Mach numbers and angles of attack.

The results of these simulations are shown in Figure 10, where they are plotted against the analytical solution. Per the figure, it seems the numerical solver is relatively in agreement with the analytical solution. All simulations that solved produced shocks at angles close to what was expected.

Describing the quantitative error of the numerical solver is difficult, as there are many confounding sources of error (with large propagation nonetheless). On top of the inherit inaccuracies of a numerical solver, the finite volume method makes it difficult to find a *point* that the shock travels through (used to calculated β). The finite volume method (used by the solver) only calculates cell averages for the values it is solving for, and thus the method does not provide data at a specific point. An interpolation scheme had to be used to find the location of the shock, which introduces another source of error. Furthermore, the exact location at which the shock occurs is difficult to find with cellular data, which also may increase the error. Despite the many sources of error, the results seem rather accurate.

Nevertheless, an error analysis (at Mach 3) was preformed. Several simulations were run with a varying number of cells. The time step for each simulation was adjusted such that the Courant number was approximately the same for each simulation. The results are shown in Figure 11. Both the 24,000 and 90,000 cell simulations produce less accurate results than the 360,000 cell simulation. It seems that the 360,000 cell simulation comes pretty close to the analytical solution.

However, it is not obvious as to whether the 24,000 or 90,000 cell simulation produces the more-accurate result. This is likely a result of the confounding sources of error introducing more error than the simulation itself. The 360,000 cell simulation probably has enough resolution such that the errors involved of interpolation and selection of shock location have less of an impact than the lower resolution simulations.

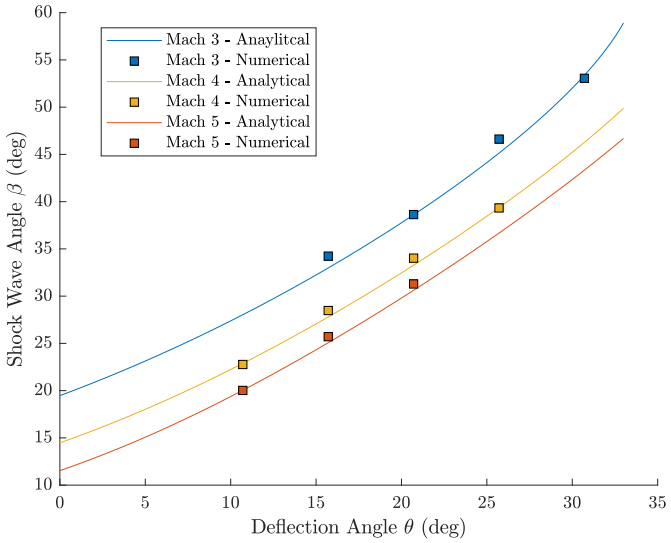

Figure 10: Analytical and numerical $\theta\beta M$ curve. Number of cells = 90,000 for all simulations.

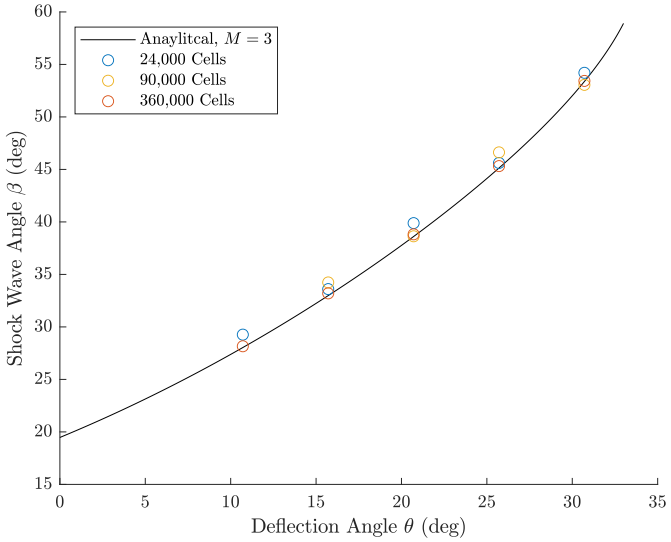

Figure 11: Convergence of the solution for various grid resolutions. The timestep was adjusted such that the Courant number was approximately the same for all simulations.

It is worth noting that the lower resolution meshes result in values for β slightly above the analytical solution. This is most likely a result of potential bias introduced by the script used to determine the location of the shock rather than an error from the solver itself. The shock occurs (is smeared) throughout several cells, so determining the exact location of the shock wave without bias is difficult.

In retrospect, it may have been best to generate Figure 10 using the 360,000 cell meshes. The data in Figure 10 would have been more accurate, but there would be in an increase in runtime nearly proportional to the number of cells. The 90,000 cell simulations for Figure 10 had runtimes of one to two hours with 64 processes, so simulations with four times as many cells would have around four times the runtime. Since nearly a dozen simulations were used to generate the data for the figure, it would have been very computationally expensive to generate the data using the 360,000 cell mesh.

6 References

Anderson, John D. *Modern Compressible Flow: With Historical Perspective.* Boston: McGraw-Hill, 2003. Print.

Link to repository: `https://github.com/bradenpecora/diamond-airfoil`